JGR Space Physics

RESEARCH ARTICLE
10.1029/2021JA029516

Special Section:
Cluster 20th anniversary: results from the first 3D mission

Hot Plasma in the Magnetotail Lobes Shows Characteristics Consistent With Closed Field Lines Trapped in the Lobes

John C. Coxon[1], Robert C. Fear[1], Jade A. Reidy[2], Laura J. Fryer[1], and James Plank[1]

[1]School of Physics & Astronomy, University of Southampton, Southampton, UK, [2]British Antarctic Survey, Cambridge, UK

Key Points:

- We identify field lines that are open according to the T96 model, but which have anomalously hot plasma
- The temperature of the plasma increases toward the center of the magnetosphere and away from Earth
- We interpret this as evidence for closed field lines trapped in the lobe during mainly northward Interplanetary Magnetic Field

Supporting Information:

Supporting Information may be found in the online version of this article.

Correspondence to:

J. C. Coxon,
work@johncoxon.co.uk

Citation:

Coxon, J. C., Fear, R. C., Reidy, J. A., Fryer, L. J., & Plank, J. (2021). Hot plasma in the magnetotail lobes shows characteristics consistent with closed field lines trapped in the lobes. *Journal of Geophysical Research: Space Physics*, *126*, e2021JA029516. https://doi.org/10.1029/2021JA029516

Received 30 APR 2021
Accepted 27 JUL 2021

Abstract We examine the magnetotail using data from the Hot Ion Analyzer on Cluster 1 during 2001–2009. We develop and utilize an algorithm in order to identify times during which Cluster 1 is in the magnetotail lobe but observes plasma, which is hotter than our expectations of the lobe. We analyze the prevailing Interplanetary Magnetic Field (IMF) B_Z conditions for our algorithm and a reference algorithm (with no particle energy criteria) and find that the periods we select are, on average, ~2 nT more toward northward IMF. Examining the temperature in the magnetotail for our periods shows that the morphology of the average temperature is consistent with the Milan et al. (2005, https://doi.org/10.1029/2004JA010835) model of a magnetotail structure during northward IMF, in which closed field lines are prevented from convecting to the dayside, causing them and the plasma trapped on them to protrude into the magnetotail lobes. We also find evidence that ~0.5% of our identified periods may be driven by direct entry into the magnetosphere from the solar wind.

Plain Language Summary We use data from a four-spacecraft mission called Cluster to measure charged particles in Earth's magnetic field, on the night side of the Earth. We look for regions in which there would usually not be many charged particles, or these particles would not be very hot, and then look for times when the particles are hotter than we expect. We analyze these periods by looking at how different variables are distributed during these periods, and we use this to differentiate between two ideas which have been proposed to explain this sort of particle signature.

1. Introduction

The configuration of the magnetosphere during southward Interplanetary Magnetic Field (IMF) is well-understood, and was first described by Dungey (1961). Magnetic reconnection between the IMF and Earth's magnetic field converts field lines from a closed to an open topology and causes them to convect tailward; magnetic reconnection occurs in the magnetotail, which closes these open field lines, and they move toward Earth and then convect around the planet, back to the dayside. As the plasma is frozen into the magnetic field, plasma on closed field lines cannot escape those field lines; but plasma on open field lines can escape into the solar wind. The magnetotail lobes comprise the regions of open field lines to the north and to the south of the plasma sheet. In general, this means that the magnetotail lobes have more tenuous, colder plasma than the closed field lines comprising the plasma sheet.

This simple picture explains why aurora are seen in ovals encircling the open flux at the poles, but does not explain the times when arcs are seen poleward of the main auroral region. Berkey et al. (1976) showed that these arcs are seen during northward IMF, in contrast to the simple picture outlined by Dungey (1961). Zhu et al. (1997) presented a review of polar cap arcs, outlining one potential magnetotail configuration in which closed field lines get trapped in the magnetotail (unable to convect around Earth) and these field lines intrude upon the polar cap as a result, causing transpolar arcs; this is consistent with Frank et al. (1982, 1986) observations of open field lines on either side of a transpolar arc on closed field lines. Another potential configuration outlined by Zhu et al. (1997) is the direct entry of plasma into the lobe caused by magnetic reconnection at the high-latitude magnetopause (e.g., Gosling et al., 1996; Le et al., 1996; Song & Russell, 1992). A recent review of transpolar arcs can be found in Hosokawa et al. (2020).

Milan et al. (2005) suggested a mechanism which could result in a transpolar arc configuration. When the IMF is northward and there is a B_Y component in Earth's magnetotail (e.g., Browett et al., 2017; Coxon et al., 2019; Tenfjord et al., 2015), return flows due to newly closed field lines will be asymmetrical about midnight (Grocott et al., 2003, 2007). In the Milan et al. (2005) mechanism, closed flux builds up due to a stagnation of the return flows due to duskward and dawnward components of the returning force approximately canceling, and observations have been presented which are consistent with this mechanism (Goudarzi et al., 2008). Therefore, hot plasma can be seen on closed field lines, which are in the magnetotail lobes.

A survey of times in which anomalously hot plasma was seen in the magnetotail lobes was previously conducted by Shi et al. (2013). The authors were specifically looking for magnetosheath or cusp-like ions, and their method was designed to exclude plasma sheet-like ions (with higher energies) and upflowing ions from the ionosphere (with lower energies). Shi et al. (2013) concluded that the anomalously hot plasma identified by their algorithm was a result of direct entry of plasma into the lobe caused by magnetic reconnection at the high-latitude magnetopause by comparing the density of the plasma they identified with the solar wind density, interpreting a high correlation between the densities as evidence for this model. We note that they also did not eliminate impulsive penetration as a mechanism (Woch & Lundin, 1992).

A key testable difference between the Milan et al. (2005) mechanism and the direct entry mechanism is that the source of the plasma is different between the two; in the former, the plasma will be from the plasma sheet, whereas in the latter, it will be from the solar wind. It is this difference that we test in this study. Another key difference is that in the Shi et al. (2013) mechanism, the hot plasma will have an auroral signature in a single hemisphere, whereas the Milan et al. (2005) mechanism will give rise to conjugate auroral signatures. The time scales in the magnetosphere are also pertinent: the direct entry model implies an instantaneous interaction between the solar wind and the magnetosphere (hence, the instantaneous correlations employed in Shi et al., 2013). Counter to this, the closed field line model is dependent on the time history of the solar wind-magnetosphere coupling that has led to the trapped field lines (Fear & Milan, 2012a, 2012b; Milan et al., 2005).

In the Milan et al. (2005) model, field lines are opened and added to the lobes asymmetrically during non-zero IMF B_Y conditions, and these field lines take timescales of 3–4 h to convect to the magnetotail. When open field lines close due to magnetotail reconnection in the ordinary Dungey cycle (Dungey, 1961), return flows cause these newly-closed field lines to convect around the polar cap to the dayside. In the case described by Milan et al. (2005), the duskward and dawnward components of the returning force cancel and so the closed field line cannot convect around the polar cap, instead extruding into the polar cap and forming a transpolar arc; thus the location of the formation of the arc is correlated with the IMF conditions 3–4 h prior to formation (Fear & Milan, 2012a). At this point, the motion of the transpolar arc is governed by the instantaneous IMF conditions (Fear & Milan, 2012a; Milan et al., 2005).

Fear et al. (2014) presented a case study of anomalously hot electrons and ions in the magnetotail lobes using Cluster data in order to differentiate between the Milan et al. (2005) and Shi et al. (2013) mechanisms. They demonstrated that this hot plasma was on closed field lines which were located at higher latitudes than the typical plasma sheet, and noted that this was consistent with the idea of a closed field line trapped in the magnetotail lobe. They used Imager for Magnetopause-to-Aurora Global Exploration (IMAGE) data to show that there was a transpolar arc simultaneous with the Cluster observations, and demonstrated that the Cluster footprint was coincident with the arc using the T96 model (Tsyganenko, 1996). Fear et al. (2014) concluded that the hot plasma was a signature of a closed field line trapped in the lobe (Milan et al., 2005), rather than direct entry due to high-latitude reconnection (Shi et al., 2013).

Fear and Milan (2012a, 2012b) showed that the statistics of transpolar arcs are consistent with the Milan et al. (2005) mechanism. In the Milan et al. (2005) mechanism there will be conjugate auroral signatures, and interhemispheric observations and surveys of transpolar arcs have observed these (Carter et al., 2017; Reidy et al., 2018; Xing et al., 2018). It has been shown in case studies (Reidy et al., 2017, 2020) that observed polar cap auroras can be driven by both a trapped-closed-field-line mechanism (Milan et al., 2005) and also by polar rain on open field lines (Zhu et al., 1997), showing that complex magnetotail configurations can

exhibit multiple behaviors simultaneously. Milan et al. (2020) were able to make inferences about the distant magnetotail during transpolar arcs by finding a conjunction with a solar wind pressure step.

Nakamura, Eriksson, et al. (2017) modeled Kelvin-Helmholtz interactions and found that they could allow direct solar wind plasma entry to the magnetosphere during strongly northward IMF conditions. Nakamura, Hasegawa, et al. (2017) demonstrated that MMS data were consistent with the modeling, and Ling et al. (2018) presented Geotail observations of Kelvin-Helmholtz waves during northward IMF. Sorathia et al. (2019) modeled northward IMF and noted that the modeled plasma entry rates were consistent with Shi et al. (2013).

Recently, Fryer et al. (2021) examined three case studies of anomalously hot plasma in the lobe and concluded they were consistent with the Milan et al. (2005) mechanism. The authors outlined a key testable difference in the predictions of the two models, concerning the configuration of the magnetotail in each mechanism (see their Figure 1 for a schematic diagram of this configuration). In the Milan et al. (2005) model, the hot plasma lies on field lines that have recently closed due to nightside reconnection are therefore contracted compared to their pre-reconnection configuration. In the Shi et al. (2013) model, field lines reconnect at the high-latitude magnetopause. These field lines will initially contract toward the Earth, at which point the plasma will be hottest, before stretching out again toward the nightside due to the convection during northward IMF (Cowley, 1981). This therefore means that Milan et al. (2005) predicts the hottest plasma in the lobes should be on field lines further from the magnetopause and closer to the plasma sheet, whereas Shi et al. (2013) predicts the hottest plasma should be on field lines closer to the magnetopause.

This brings us to the open question we focus on herein. Is anomalously hot plasma observed in the magnetotail lobes generally a result of trapped closed field lines unable to convect around Earth due to asymmetries in return flow during northward IMF? Or is it generally a result of direct entry into the magnetotail during periods of high-latitude reconnection during northward IMF? The object of this study is to examine this question statistically, and to do so using an algorithm that can capture the full range of anomalously hot plasma in the lobes.

In Section 2, we describe the data we use and the manner in which the data were obtained, as well as our replication of the Shi et al. (2013) algorithm. In Section 3, we conceive our own technique for identifying these times, and present the results thereof. We discuss the results in Section 5.

2. Data

We use data from the Cluster constellation, comprising four satellites in polar orbit with a perigee of ~$4R_E$ and an apogee of ~$19.5R_E$ (C. Escoubet et al., 1997; C. P. Escoubet et al., 2001). We obtained data from the Cluster Ion Spectrometer (CIS) Hot Ion Analyzer (HIA) (Rème et al., 2001) and the Fluxgate Magnetometer (FGM) (Balogh et al., 2001) from the Cluster Science Archive (Laakso et al., 2010). We calculate plasma beta by combining the HIA and FGM data. Additionally, we use data from the European Cluster Assimilation Technology (ECLAT) data set. also downloaded from the Cluster Science Archive. From ECLAT, we use FUV imager data from the IMAGE spacecraft (Mende, Heetderks, Frey., Lampton, Geller, Abiad, et al., 2000; Mende, Heetderks, Frey, Lampton, Geller, Habraken, et al., 2000), and Cluster footprints mapped from the location of the spacecraft using the T96 model (Tsyganenko, 1996). Finally, we employ the OMNI HRO data set at a cadence of 1 min, specifically IMF data in GSM coordinates, the proton density, and the flow speed (King & Papitashvili, 2014). All data were obtained for the time period 2001–2009 except IMAGE data, which were obtained for 2001–2005.

We use the event list used in Shi et al. (2013) in order to compare our replication of their algorithm for the comparisons herein. Shi et al. (2013) used Cluster data and looked for times during which the particle energy flux in the energy band 700–2,000 eV was greater than 8×10^4 keV s^{-1} cm^{-2} sr^{-1} keV^{-1}. In addition, they discarded times at which plasma beta was above 0.05, $\left|Z_{GSM}\right| < 5R_E$, and $\left|Y_{GSM}\right| < 10R_E$ to try to exclude times when the Cluster spacecraft may have been in the plasma sheet. A variation of this method was described in Shi (2019), in which at least one energy band below 1 keV and one above 1 keV, and in which at least six energy bands in total, must have exceeded the same target particle energy flux threshold. In order to replicate the event list in Shi et al. (2013) it is necessary to adopt criteria on top of the description of the

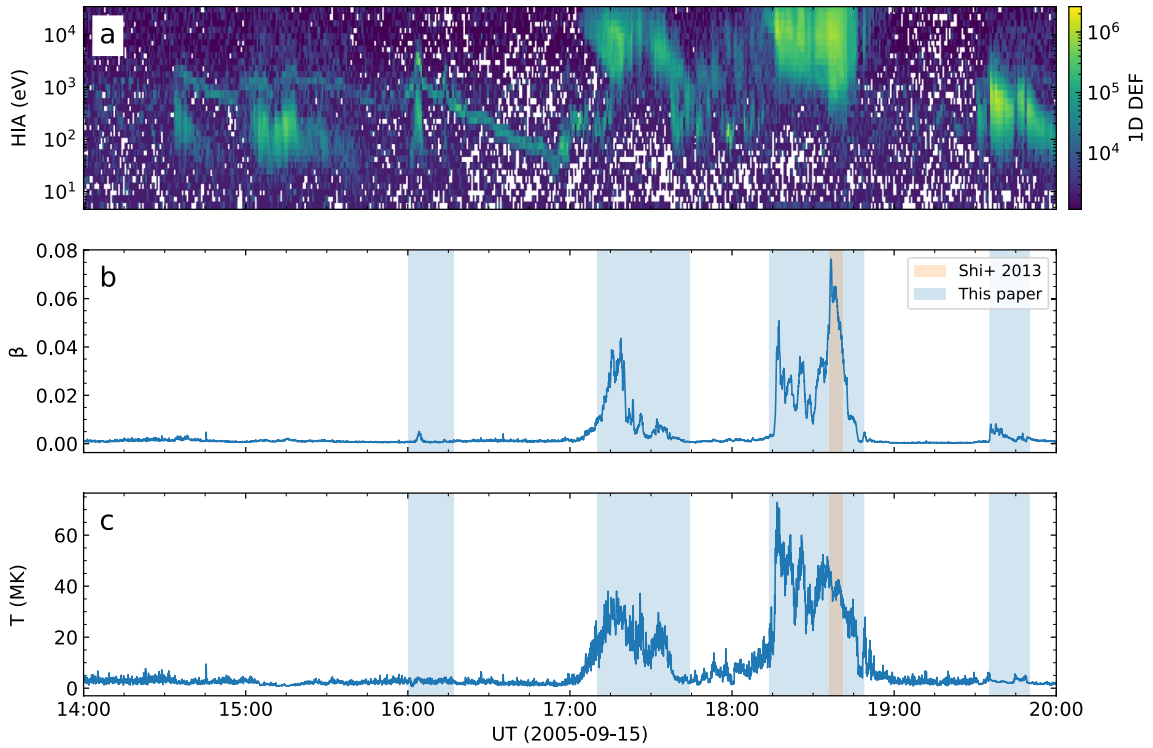

Figure 1. Cluster 1 Cluster Ion Spectrometer-Hot Ion Analyzer data for 14:00–20:00 on September 15, 2005, showing (a) differential energy flux; (b) plasma beta; and (c) temperature. Orange shading shows the algorithm of Shi et al. (2013) applied to this period (see Section 2) and blue shading shows the algorithm described in Section 3.

algorithm within that study; namely, we concatenate periods that are separated by <10 min and then discard periods < 5 min long, which achieves the best correspondence with the provided event list.

3. Periods of Interest

In order to compare the Shi et al. (2013) algorithm and Fear et al. (2014) observations and highlight our motivation for the development of the algorithm herein, we present the case study of Fear et al. (2014) in Figure 1. Figures 1a and 1c show the ion differential energy flux (in keV cm^{-2} s^{-1} str^{-1} keV^{-1}) and temperature (in MK), replicating their Figures 2d and 2e respectively. Additionally, we plot plasma beta in Figure 1b. Orange highlighting shows the results of the Shi et al. (2013) algorithm applied to this period, and illustrates that although the data therein is not from the true plasma sheet, the high fluxes are at energies too high to be identified by that algorithm. The fact that the Shi et al. (2013) only identifies a very small subset of this event indicates that this algorithm will not identify the full range of events we wish to capture.

Because we wish to examine all periods in which hot plasma appears to be trapped in the lobe, we adopt a different approach to previous statistical studies of the magnetotail (Shi et al., 2013). We adopt the same particle energy flux criterion, specifying that our fluxes of interest are those greater than 8×10^4 keV s^{-1} cm^{-2} sr^{-1} keV^{-1}, but we look for times at which this flux was exceeded at any energy level above 700 eV. We do not control for plasma beta and we do not set an upper energy threshold on our flux criterion, in order to avoid excluding periods of interest. In order to ensure that we do not contaminate our results with data in the true plasma sheet or magnetosheath, we adopt $|Y_{GSM}| < 10R_E$ and $|Z_{GSM}| > 5R_E$ criteria and also require that Cluster is on open field lines (i.e., has a single footprint on Earth's surface) according to the T96 field line traces in ECLAT. Statistical studies of plasma sheet flapping indicate that excluding data in the region $|Z_{GSM}| \leq 5R_E$ will exclude contamination due to flapping (Davey, Lester, Milan, & Fear, 2012; Davey, Lester, Milan, Fear, & Forsyth, 2012). We specify that our periods must occur between 1 August and

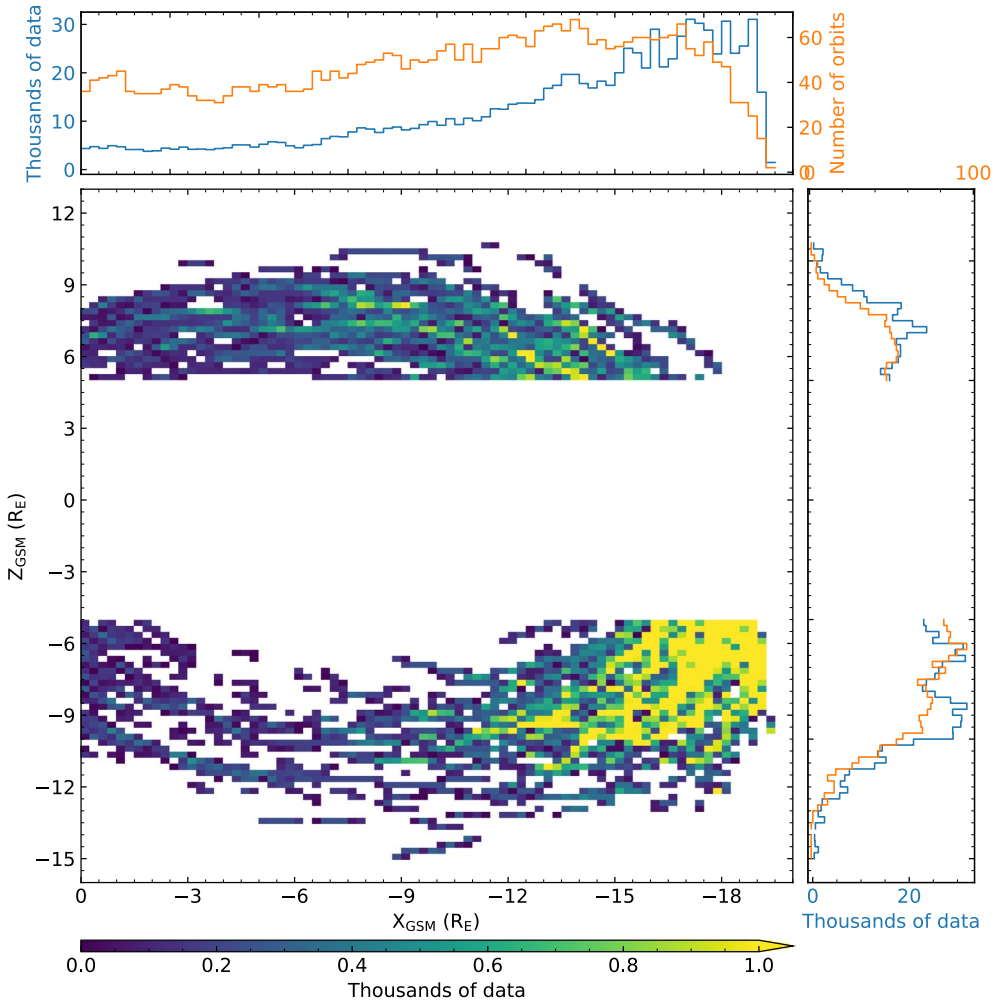

Figure 2. Main: The GSM *XZ* plane, color-coded by the number of data per bin (at spin cadence) observed by Hot Ion Analyzer between 2001 and 2009. The number of data on the color bar is expressed in thousands of data (e.g., 0.2 is 200 data). White indicates there are no data in that bin. Top: The number of data per *X* bin (blue) and number of orbits contributing to each (orange). Right: as for the top, but per *Z* bin.

9 October (inclusive), which limits our observations to the "tail season" (the period of time where Cluster's apogee is located at $X \sim -20R_E$ and $Z \sim 0R_E$).

To summarize our algorithm, we flag any period in which each of the following criteria is met between 1 August and 9 October (inclusive) in each year:

1. Particle flux at any energy level above 700 eV exceeds 8×10^4 keV s^{-1} cm^{-2} sr^{-1} keV^{-1} according to HIA.
2. $|Y_{GSM}| < 10R_E$.
3. $|Z_{GSM}| > 5R_E$.
4. Cluster is on open field lines according to the ECLAT T96 traces.

We then concatenate periods that are separated by <10 min and then discard periods < 5 min long. Figure 1 shows how much more of the event is identified by our criteria than by the Shi et al. (2013) method.

Applying our criteria for 2001–2009 results in 1,330 periods in which all of our criteria are met (a full list is made available in Supporting Information S1). A histogram of the number of data (at spin cadence) measured in these periods is presented in Figure 2. The number of data is larger with distance downtail and inversely proportional to distance in $|Z|$; the downtail variation is less pronounced in the Northern Hemisphere than in the Southern Hemisphere. The number of orbits contributing to each bin follows the same

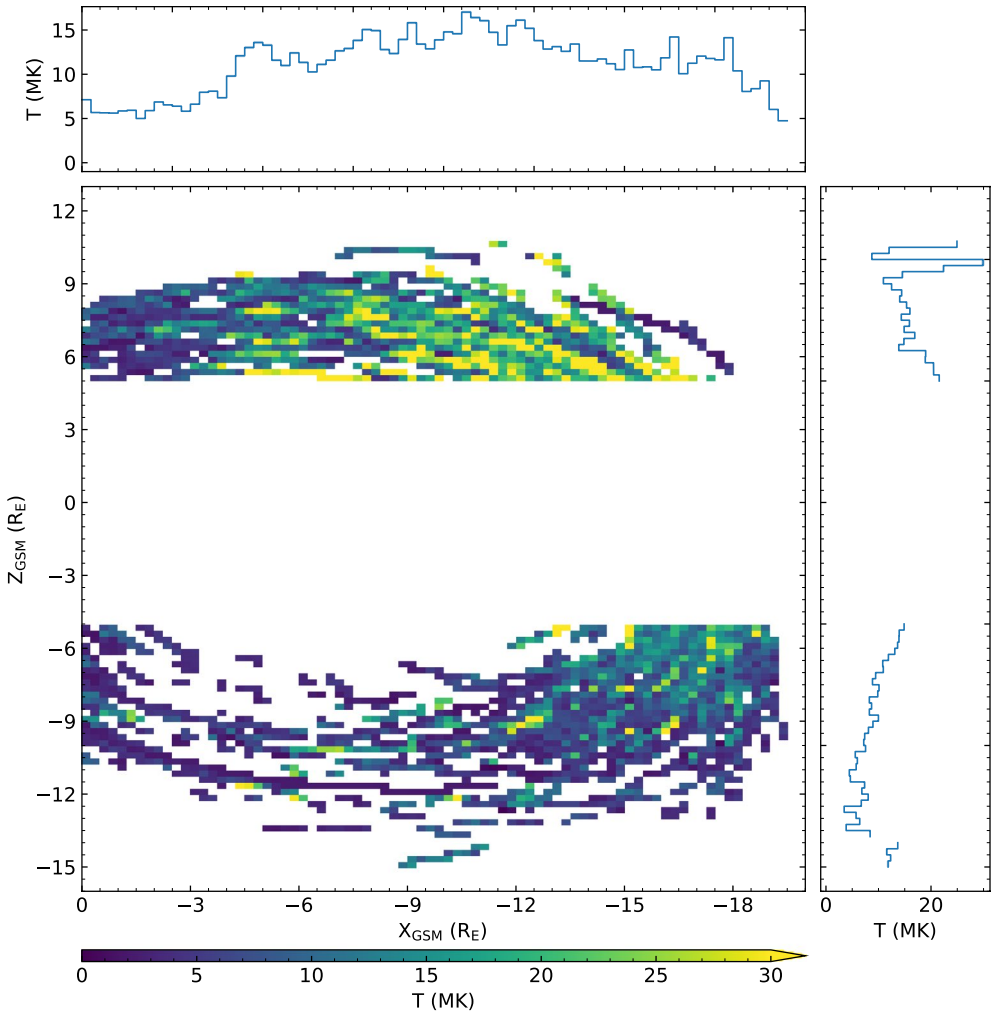

Figure 3. Main: The GSM *XZ* plane, color-coded by the average temperature per bin observed by Hot Ion Analyzer between 2001 and 2009. White indicates there are no data in that bin. Top: The average temperature per X bin. Right: as for the top, but per Z bin. In the top and right panels, shading shows the standard error on the mean (this is very small and may therefore not be visible).

trends with the exception of $X < -15R_E$, at which point the number of orbits drops off. This is consistent with the orbit of Cluster during the tail season; the spacecraft spends more time at apogee but fewer orbits intersect extreme downtail distances.

Figure 3 shows the temperature distribution in the periods identified by our algorithm (We exclude any temperature higher than 1 GK from our analysis as erroneous, which discards ~ 0.0015% of the data). Going downtail, the average temperature increases from 5 MK at $X = 0R_E$ to 17 MK at $X = -12R_E$, decreases slowly to 10 MK by $X = -18R_E$ and then decreases quickly to 5 MK by $X = -20R_E$. In the Northern Hemisphere, the average temperature at $Z = 5R_E$ is 20 MK, decreasing to 10 MK by $Z = 9R_E$. In the Southern Hemisphere, the average temperature at $Z = -5R_E$ is 15 MK, decreasing to 5 MK by $Z = -11R_E$. In both hemispheres, the temperatures at the very edge of the distribution spike; to 25 MK at the extreme of the Northern Hemisphere and 15 MK at the extreme of the Southern Hemisphere.

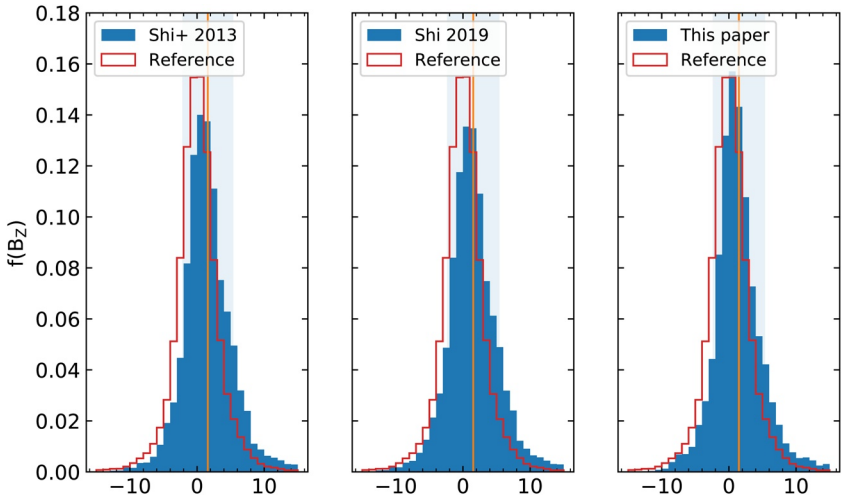

Figure 4. Histograms showing the distribution of Interplanetary Magnetic Field B_Z (in GSM coordinates) for (left) Shi et al. (2013), (middle) Shi (2019), and (right) the algorithm described in this study. Red lines are identical in each panel, and show the distribution of the same data using a "reference" approach described in the text. The orange line describes the mean B_Z of each distribution, and the shaded area describes the standard deviation.

4. Correspondence With the IMF

Figure 4 shows the distribution of IMF B_Z for the periods identified by our algorithm, and also those identified by the algorithms in Shi et al. (2013) and Shi (2019). The orange lines show the distribution of IMF B_Z for a reference algorithm, in which we relax the criteria on the Z coordinate, T96 trace and particle energy flux threshold but maintain the criteria in space ($X < 0R_E$ and $|Y| < 10R_E$) and in time (between 1 August and 9 October of each year); the orange line is symmetrical and peaks at 0 nT, representing the background IMF distribution for the period we investigate. The fraction of B_Z is lower than the reference distribution for $B_Z < 0$ nT and higher for $B_Z > 0$ nT for all three algorithms, and the mean of each is positive, indicating that each distribution is biased toward northward IMF.

Figure 5 shows the mean IMF B_Z for the Shi et al. (2013) and Shi (2019) algorithms (in blue and orange) alongside the algorithm described in this paper (in green) and the reference algorithm (in red), where time lags of 0–6 h have been applied to the IMF. The mean B_Z for the reference algorithm does not exceed 0.05 nT at any time lag. The algorithm in this paper reaches a maximum mean of 1.94 nT at a time lag of 1 h, and the Shi et al. (2013) and Shi (2019) algorithms both exceed a mean of 2 nT at time lags of 1–1.5 h.

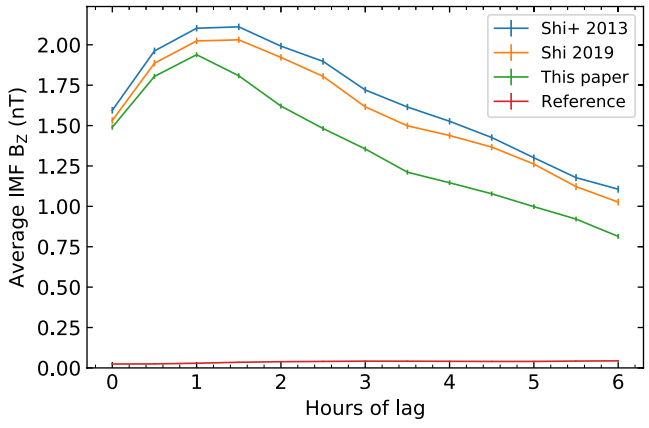

Figure 5. Mean Interplanetary Magnetic Field B_Z during 2001–2009 for time lags up to 6 h for the Shi et al. (2013) and Shi (2019) algorithms (blue and orange), alongside the algorithm described in this paper (green) and the reference algorithm (red). Error bars indicate the standard error on the mean.

Figure 6 shows temperature data presented similarly to Figure 3, but subsetting by IMF condition (in this case, setting $B_Y < 0$ nT) and shifting from the XZ plane to the YZ plane in GSM coordinates. In the top panel, the average temperature in each Y_{GSM} bin is plotted separately for the Northern and Southern Hemispheres. We can see from this figure that the largest temperatures for this IMF condition are seen in the Northern Hemisphere at negative values of Y_{GSM} and are seen in the Southern Hemisphere at positive values of Y_{GSM}. The relationship in the Z direction is the same as in Figure 3: that is, it is the same as without imposing the IMF restriction.

Figure 7 shows temperature data as for Figure 6 but in this case for IMF $B_Y > 0$ nT. We can see that the number of bins in this case is smaller than for negative B_Y, indicating that negative B_Y dominated during the interval under discussion. We interpret this as a signature of an interplay between the Parker spiral (Parker, 1957, 1958) and an orbital selection effect. In the GSE coordinate system, the IMF B_X and B_Y components

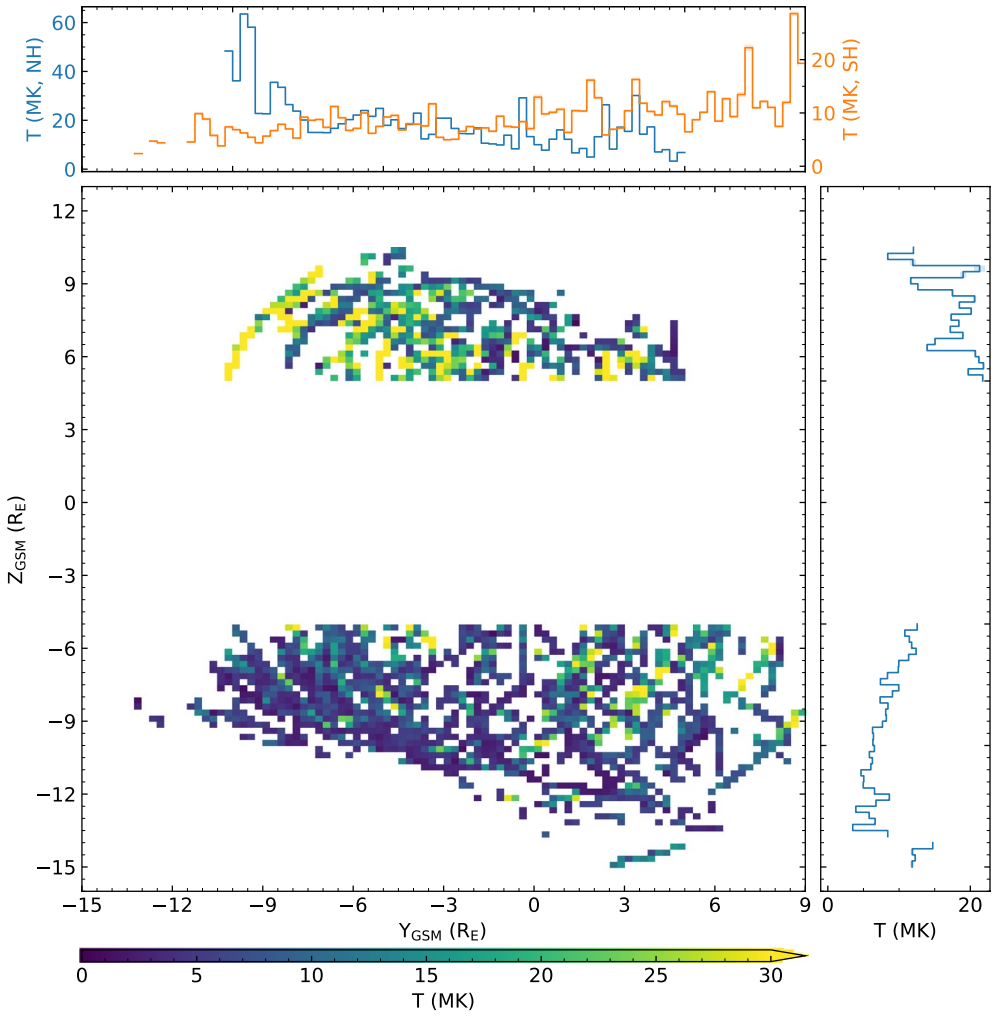

Figure 6. Main: The GSM *YZ* plane for periods in which $B_Y < 0$ nT, color-coded by the average temperature per bin observed by Hot Ion Analyzer between 2001 and 2009. White indicates there are no data in that bin. Top: The average temperature per Y_{GSM} bin for the Northern Hemisphere (blue) and the Southern Hemisphere (orange). Right: as for the top, but per Z_{GSM} bin for all data. In the top and right panels, shading shows the standard error on the mean.

are anticorrelated as a result of the Parker spiral (Ness & Wilcox, 1964). Because our observations were made between 1 August and 9 October in each year, we are biased toward observations around the September equinox, and so throughout these periods the component of Earth's dipole tilt in the GSE *YZ* plane is consistently inclined toward the $-Y$ axis. Because we are using GSM coordinates for the IMF, and these are defined by Earth's dipole, this introduces a correlation between IMF B_Y and B_Z: negative B_Y will be correlated with positive (northward) B_Z and vice versa. Since our algorithm selects periods characterized by northward IMF (Figures 4 and 5), this means that it will also predominantly select negative B_Y, explaining the observed dominance.

This is plotted in Figures 8 (top) and 9 (left), which show the clock angle distributions for the algorithm we employ (in blue) and for the reference algorithm used in Figure 4 (in red). Figure 8 (top) demonstrates in red that there is clearly a bimodal distribution in the clock angle distribution during the seasons we examine, as expected. Figure 9 (left, also in red) shows that this is tilted such that southward IMF is associated with duskward IMF ($B_Y > 0$ nT) and northward IMF with dawnward IMF ($B_Y < 0$ nT) in GSM coordinates, as we outline above.

Figures 8 (top) and 9 (left) also show the IMF distribution of the events selected by our algorithm plotted underneath the reference algorithm. There is a tendency for events to be identified during northward and

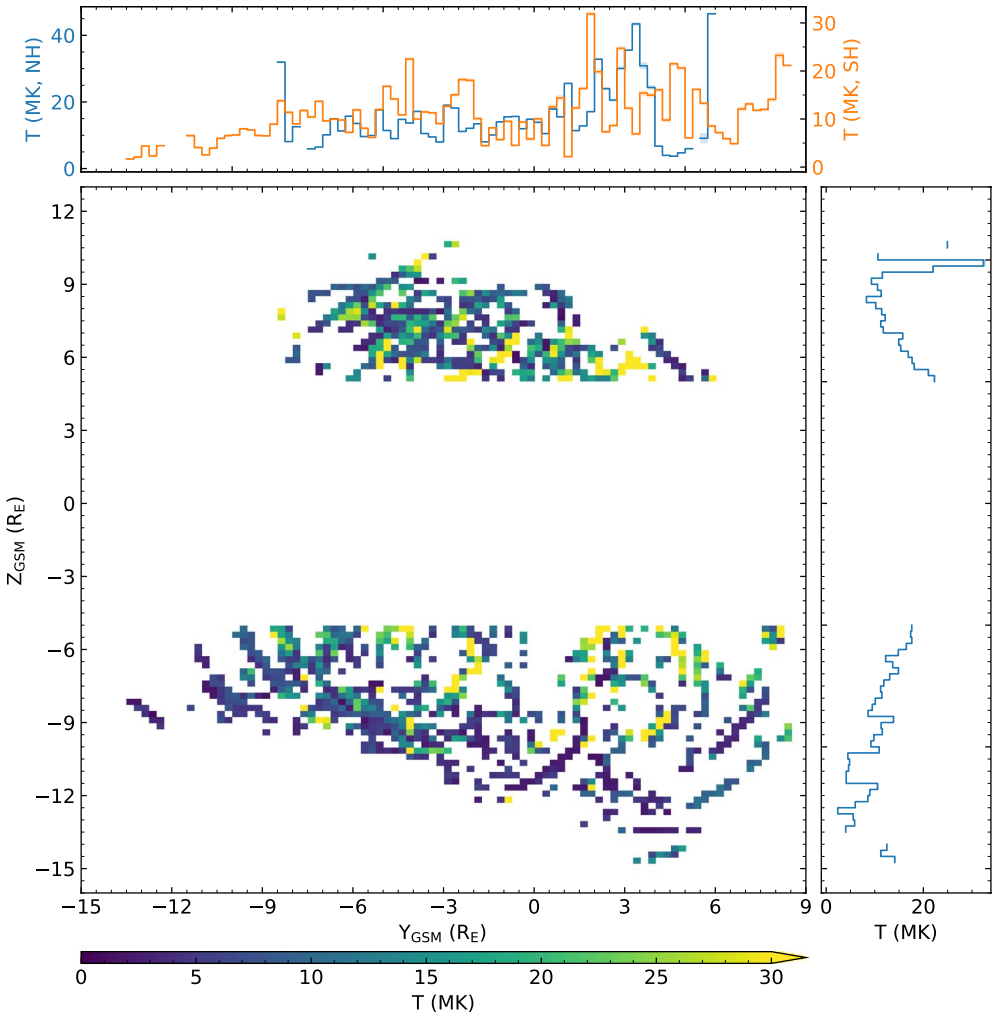

Figure 7. As Figure 6, but for $B_Y > 0$ nT. In the top and right panels, shading shows the standard error on the mean.

dawnward IMF. Figures 8 (bottom) and 9 (right) show the distribution normalized by dividing it by the reference distribution and expressing this as a percentage. The normalized distribution is biased more generally toward northward IMF; although there is still a level of bias toward dawnward IMF, this is reduced relative to the unnormalized data. Therefore, the selection effects we observe (blue areas on the left/top) are due to a combination of prevailing IMF distribution (red outline on the left/top) and a preference for northward IMF selection (blue areas on the right/bottom).

This accounts for much less smooth relationships between temperature and location, both in the Y_{GSM} direction and (to a lesser extent) in the Z_{GSM} direction. In the Northern Hemisphere, we tentatively infer that the temperatures are getting larger toward more positive values of Y_{GSM}, but in the Southern Hemisphere we do not see a clear trend. The relationship in Z_{GSM} is in the same sense as that in Figures 3 and 6, but is much clearer in the Northern Hemisphere than in the Southern Hemisphere, which reinforces the difficulty in drawing inferences from these sparser data.

5. Discussion

In this section, we interpret our results and discuss the likelihood of the plasma we detect in the lobe arising as a result of direct entry from the solar wind (e.g., Shi et al., 2013 and references therein) as opposed to arising as a result of field lines which cannot convect back to the dayside (e.g., Fear et al., 2014 and references therein). We plotted the IMF distribution for the events mentioned above in Figures 4 and 5. In

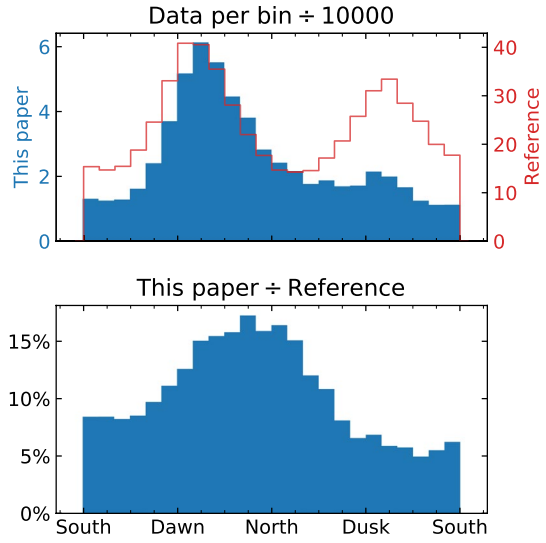

Figure 8. The distributions of clock angle θ. Top: The histogram of the clock angle distribution divided by 10,000, for the algorithm described in this study (as blue bars), and the reference algorithm (as a red line). Bottom: The histogram of the clock angle distribution for the algorithm in this paper normalized by dividing it by the histogram of the reference algorithm, expressed as a percentage.

both, it was evident that the mean IMF was significantly biased toward northward IMF conditions for all the methods discussed herein, which is consistent with both the mechanisms under discussion (Fear et al., 2014; Shi et al., 2013).

5.1. Direct Entry From the Solar Wind

Shi et al. (2013) presented evidence that the density of the solar wind was correlated with the density of anomalously hot plasma in the magnetotail during the periods they identified and argued that this meant that the periods they saw were indicative of direct entry from the solar wind. However, the correlation they quoted of $R = 0.86$ was that of the binned means rather than that of the raw data (i.e., it was achieved by taking the mean density from OMNI and from Cluster for each of their periods, and then taking the mean Cluster density in 3 cm^{-3} bins of OMNI density and computing the correlation of the mean of the means). Figure 10 shows the correspondence of the density from OMNI versus the density from C1 for each of the intervals identified by our algorithm. We perform linear regression to calculate the correlation coefficient, the error and p-value thereof, and the gradient and intercept of the regression line (plotted as dashed lines). The correlation of the mean OMNI and C1-observed density in each event is 0.361 ± 0.001, and performing the same binning in the OMNI data as that performed by Shi et al. (2013) yields a correlation of $R = 0.712 \pm 0.002$.

There are two key things to discuss here. First, the instantaneous correlation of the mean of the means here has dropped 0.15 from the result reported in Shi et al. (2013), to 0.71; this may indicate that the subset of the Cluster mission used in the previous analysis was less robust to this sort of analysis compared to using a larger time period. Notably, this correlation is not significant at the 3σ significance level ($p = 0.031$), which indicates that we cannot reject the null hypothesis that these quantities are in fact uncorrelated, providing further evidence that this behavior is not primarily driven by direct entry. Second, the correlation between the means of events is $R = 0.361$. This is significant at the 3σ level ($p = 1.2 \times 10^{-35}$), but means that only 13% (R^2) of the variability is governed by the solar wind density. We argue that it does not provide convincing evidence for direct entry by the solar wind, since a correlation could equally be explained by a higher solar

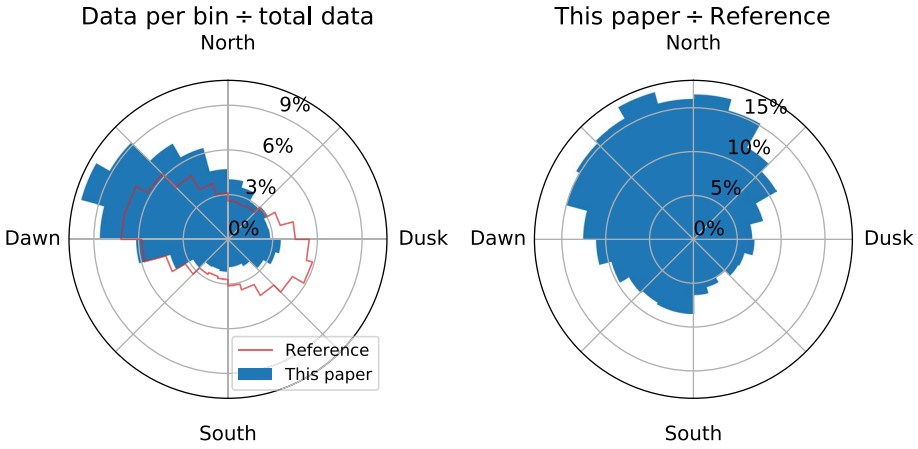

Figure 9. The distributions of clock angle θ. We plot these data in polar coordinates to make it easier for the reader to see the directionality of the data. The radius of the wedges here is proportional to the percentage of the data in each bin, but because the area of the wedge does not scale linearly with radius, a wedge with twice the area does not imply into a wedge with twice the data. Left: The histogram of the clock angle distribution divided by the total number of data described by the histogram, corresponding to Figure 8 (top). Right: The data from Figure 8 (bottom).

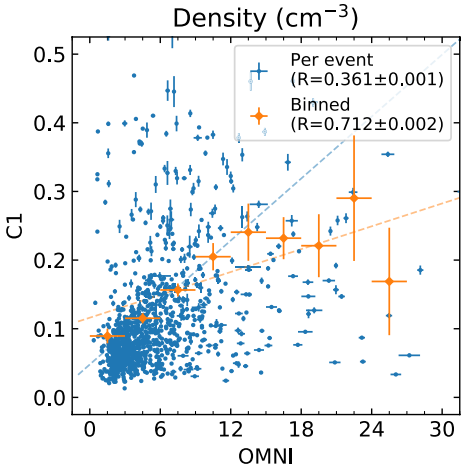

Figure 10. For each of the periods identified in this study, we take the mean of the density as reported by OMNI and by C1, and plot those means in blue, with blue error bars describing the standard error on the mean. The orange diamonds describe the mean of the C1 means in regular bins of OMNI data; the orange error bars in the *x*-axis describe the width of the OMNI bins, whereas the orange error bars in the *y*-axis describe the standard error on the mean of the means. Dashed lines are the fit lines returned by linear regression. Bins with fewer than three data are not shown and do not contribute to the quoted correlations. The text describes the statistical significance of the quoted correlation coefficients. We applied no further lag to the OMNI data.

wind density leading to a more compressed magnetosphere, which leads to a slightly higher magnetotail density (Repeating the analysis on the event list used in Shi et al., 2013 yields a similar, low correlation between the per-event mean density as opposed to the mean of the means.).

5.2. Closed Field Lines Trapped in the High-Latitude Magnetotail

The results in Section 3 show the temperature of the anomalously hot plasma identified by our algorithm within the magnetotail. If the hot plasma we detect is entering the magnetotail through direct entry from the solar wind during high-latitude reconnection, we would expect the lobe temperature to be highest nearer the magnetopause. If the hot plasma we detect is on closed field lines that cannot convect to the dayside because they are being trapped by magnetotail twisting and the absence of convection, as in the Milan et al. (2005) model, we expect the lobe temperature to be higher toward the equatorial plane of the magnetotail. This is due to the different magnetotail configurations outlined in Section 1 (Fryer et al., 2021).

Figure 3 shows that the temperatures in the magnetotail are generally largest between $-12 \geq X \geq -18R_E$ and in the Z-axis, they generally increase toward the center of the magnetotail. This is consistent with where we would expect to find the hottest plasma if that plasma is stuck on field lines not convecting to the dayside in the Milan et al. (2005) paradigm.

Figures 6 and 7 show the relationship between temperature and IMF B_Y, and we find that for negative B_Y the highest temperatures are at negative Y_{GSM} in the Northern Hemisphere and at positive Y_{GSM} in the Southern Hemisphere. Milan et al. (2005) predict that in their mechanism, during negative B_Y, TPAs will form toward dawn (i.e., toward negative Y_{GSM}) in the Northern Hemisphere and toward dusk (toward positive Y_{GSM}) in the Southern Hemisphere, which is consistent with what we see in Figure 6 and means we interpret this behavior in the context of their model. Their prediction is reversed for positive B_Y: Figure 7 is not inconsistent with this but is much less conclusive than the data for negative B_Y.

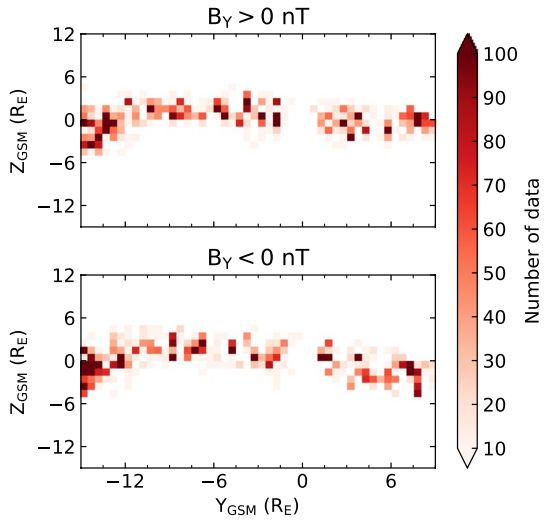

Figure 11. A histogram showing the coordinates at which C1 neutral sheet crossings were reported by Boakes et al. (2014) for negative Interplanetary Magnetic Field (IMF) B_Y (top) and positive IMF B_Y (bottom). Bins with no reported crossings are shown in white.

We note that this is also in the same sense as tail twisting, in which a prevailing B_Y condition leads to a large-scale rotation of the magnetotail, including the plasma sheet (Cowley, 1981; Grocott et al., 2007). To exclude this as an explanation, we present Figure 11. This figure shows the locations of neutral sheet crossings in the period of discussion from the method and data presented by Boakes et al. (2014). We use this as opposed to the inner/outer plasma sheet criteria presented by Boakes et al. (2014) because their plasma sheet criteria are likely also to identify the very periods of interest in this study, whereas neutral sheet crossings will only occur in the regular plasma sheet.

Figure 11 shows that the plasma sheet for negative (top) and positive (bottom) IMF B_Y are similar in shape with no obvious twist between the two. Due to orbital coverage, and given our exclusion of more equatorial regions, our northern hemisphere events all fall within the range $-10R_E < Y_{GSM} < 6R_E$ (Figures 6 and 7). In this dawn-dusk range, the neutral sheet crossings identified by Boakes et al. (2014) are mostly within the range $-4R_E < Z_{GSM} < 4R_E$. Under normal conditions, the plasma sheet has a thickness of between $0.5 - 5R_E$ (e.g., Panov et al., 2010 and references therein), corresponding to half thicknesses of $0.25 - 2.5R_E$; adding these values together provides an upper limit of the maximum Z_{GSM} displacement of the regular plasma sheet that would be expect-

Table 1
Events Contributing to High Temperatures at Extreme Z Positions

Event	Start	End
1	2001-08-07 13.09.45	2001-08-07 13.28.55
2	2001-08-14 12.58.56	2001-08-14 14.23.08
3	2002-08-06 06.33.36	2002-08-06 10.35.08
4	2006-09-26 10.56.24	2006-09-26 11.47.59
5	2006-10-06 01.02.14	2006-10-06 04.18.26
6	2006-10-08 05.16.55	2006-10-08 08.30.34
7	2009-10-04 11.23.12	2009-10-04 11.49.31

ed from magnetotail rotation in this portion of the tail as between $4.5 - 6.5R_E$. This, combined with the lack of an obvious twist, indicates that the effects seen in Figures 6 and 7 are not due to a rotation of the tail (and plasma sheet), further supporting our interpretation of asymmetric return flows due to a prevailing B_Y condition.

5.3. High Temperatures at Extreme Z Positions

We see very high temperatures in Figure 3 at $Z \geq 10R_E$ and $Z \leq -13R_E$. Figure 2 (right) shows that the bins that show these temperatures correspond to low numbers of orbits, and we investigate the events, which contribute to these high temperatures in Table 1. There are seven in all: two in 2001, one in 2002, three in 2006, and one in 2009. It does not appear that these events are due to the spacecraft entering the magnetosheath. Plots of each event in a similar format to Figure 1 are presented in Supporting Information S1.

It is possible that these seven events represent direct entry from the solar wind into the magnetotail as proposed by Shi et al. (2013). To test this, we generate an equivalent to Figure 10 using solely these events, which is presented in Figure 12. It can be seen that the correlation between the OMNI and C1-measured density is 0.986 ± 0.002, which is significant at the 3σ level ($p = 4.7 \times 10^{-5}$) despite the small number of data. From this, we can determine that the solar wind density is directly related to the density of the magnetotail during these events.

It is also possible that these events represent the spacecraft entering the magnetosheath and sampling the plasma in the sheath as opposed to the magnetotail lobes. We do not think these events are sampling the magnetosheath because, in the Supporting Information S1, the magnetic field observations from C1 (panel e in Figures S1–S7) show steady magnetic field uncharacteristic of the magnetosheath in each event. To further test this, we plot Figure 13 which compares the in situ velocity in X_{GSE} to the solar wind flow speed reported by OMNI. The magnitude of the mean plasma velocity components observed by Cluster during these events are all < 50 km s^{-1}. This is far slower than would be expected for magnetosheath flow this far downtail, with the exception of one event, which had a higher velocity but was in the sunward direction. The correlation between the solar wind flow speed and velocity observed by C1 is 0.139 ± 0.292 and is insignificant at the 3σ level ($p = 0.77$), indicating that the plasma flow sampled in these events is uncorrelated with the solar wind flow speed. We interpret this as evidence that C1 does not enter the magnetosheath and is still sampling the high-latitude lobe. Therefore, we conclude that these events are likely to be indicative of direct entry by the solar wind, potentially due to Kelvin-Helmholtz interactions (Ling et al., 2018; Nakamura, Eriksson, et al., 2017; Nakamura, Hasegawa, et al., 2017; Sorathia et al., 2019) or lobe reconnection (Cowley, 1981; Dungey, 1961; Fear, 2021 and references therein).

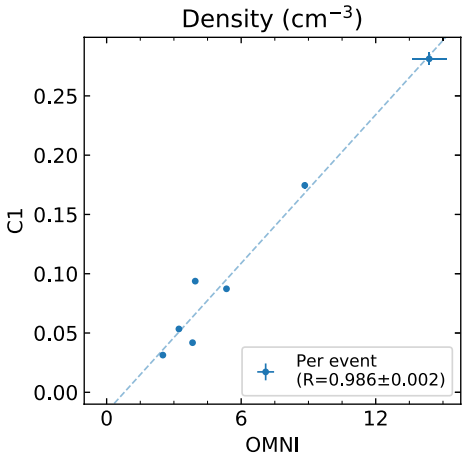

Figure 12. For each of the periods identified in Table 1, we take the mean of the density and plot it in the same format as Figure 10. We do not repeat the binning due to the small number of events. We applied no further lag to the OMNI data.

However, we note that the events listed in Table 1 comprise 0.5% of the periods we identify. We compare these events to our reference algorithm, and find that excursions into the same spatial range ($Z \geq 10R_E$ and $Z \leq 13R_E$) occur 30 times out of 243 continuous periods, which is 12.3%, 20 times higher than the occurrence rate of the events in Table 1. However, all of the events which show anomalously hot plasma in this spatial region appear to be consistent with direct entry. This indicates that when hot plasma is seen here, it is very likely to be the result of direct entry, but that direct entry events are relatively rarely observed. This is consistent with the paradigms of Kelvin-Helmholtz interactions leading to plasma mixing near the magnetopause and of high latitude magnetopause reconnection leading to plasma entry that is near the magnetopause. The latter point in particular is evidenced by the fact that the auroral signature of

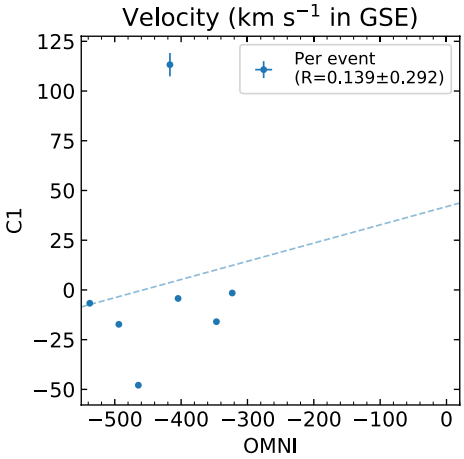

Figure 13. For each of the periods identified in Table 1, we take the mean of the velocity in the X_{GSE} direction from Cluster Ion Spectrometer-Hot Ion Analyzer and plot it in the same format as Figure 12. We applied no further lag to the OMNI data.

lobe reconnection is the cusp spot, which occurs at the sunward edge of the polar cap rather than in the more extended manner of a transpolar arc (e.g., Fear et al., 2015).

6. Conclusion

We examine the characteristics of anomalously hot plasma observed in the magnetotail lobe statistically using a new algorithm designed to capture the full range of energies. We find that the relationship between solar wind density and density in the magnetotail during each event are either weakly correlated or insignificantly correlated, indicating that direct entry from the solar wind (Shi et al., 2013) is not the primary cause of these plasma populations.

We examine the distribution of temperature through the magnetotail lobes during the events we identify and we find that the temperature generally increases toward the center of the lobes, consistent with a model in which flux that cannot convect to the dayside as a result of asymmetrical tail morphology (Milan et al., 2005). We also find that the temperatures are biased toward dawn and dusk with negative IMF B_Y conditions, consistent with the predictions of that model.

Finally, we see temperatures spike at the top and bottom of the lobes and investigate this further, finding that for seven events in this spatial range, the density in the solar wind is highly, significantly correlated with the density observed by Cluster. We interpret this as the evidence that direct entry events do occur and lead to anomalously hot plasma but are phenomena that occur very rarely (in 0.5% of our identified periods). As such, we conclude that most of the observed plasma is as a result of the mechanism put forward by Milan et al. (2005).

Data Availability Statement

Cluster data used in this study were obtained from the Cluster Science Archive at https://www.cosmos.esa.int/web/csa. OMNI HRO data at 1 min resolution were obtained from CDAweb at https://cdaweb.sci.gsfc.nasa.gov/. The Python packages used to conduct data analysis and visualization were aacgmv2 (Burrell et al., 2020; Shepherd, 2014), NumPy (van der Walt et al., 2011), Matplotlib (Hunter, 2007), SpacePy (Morley et al., 2010), and Tsyganenko (Coxon & de Larquier, 2020; Tsyganenko, 1996).

Acknowledgments
J. C. Coxon and R. C. Fear were supported by Science and Technology Facilities Council (STFC) Consolidated Grants ST/R000719/1 and ST/V000942/1. J. A. Reidy was supported by Natural Environment Research Council (NERC) Highlight Topic Grant NE/P01738X/1623 (Rad-Sat). L. J. Fryer was supported by STFC studentship ST/T506424/1 (2279917). J. Plank was supported by STFC studentship ST/V507064/1 (2502298). J. C. Coxon would like to thank A. Burrell for her expertise on AACGM coordinates.

References

Balogh, A., Carr, C. M., Acuña, M. H., Dunlop, M. W., Beek, T. J., Brown, P., et al. (2001). The cluster magnetic field investigation: Overview of in-flight performance and initial results. *Annales Geophysicae*, *19*(10/12), 1207–1217. https://doi.org/10.5194/angeo-19-1207-2001

Berkey, F. T., Cogger, L. L., Ismail, S., & Kamide, Y. (1976). Evidence for a correlation between sun-aligned arcs and the interplanetary magnetic field direction. *Geophysical Research Letters*, *3*(3), 145–147. https://doi.org/10.1029/gl003i003p00145

Boakes, P. D., Nakamura, R., Volwerk, M., & Milan, S. E. (2014). ECLAT Cluster spacecraft magnetotail plasma region identifications (2001–2009). *Dataset Papers in Science*, *2014*(11), 1–13. https://doi.org/10.1155/2014/684305

Browett, S. D., Fear, R. C., Grocott, A., & Milan, S. E. (2017). Timescales for the penetration of IMF into the Earth's magnetotail. *Journal of Geophysical Research: Space Physics*, *122*(1), 579–593. https://doi.org/10.1002/2016JA023198

Burrell, A., van der Meeren, C., & Laundal, K. M. (2020). *aburrell/aacgmv2: Version 2.6.0*. Zenodo. https://doi.org/10.5281/zenodo.3598705

Carter, J. A., Milan, S. E., Fear, R. C., Walach, M.-T., Harrison, Z. A., Paxton, L. J., & Hubert, B. (2017). Transpolar arcs observed simultaneously in both hemispheres. *Journal of Geophysical Research: Space Physics*, *122*(6), 6107–6120. https://doi.org/10.1002/2016ja023830

Cowley, S. W. H. (1981). Magnetospheric asymmetries associated with the y-component of the IMF. *Planetary and Space Science*, *29*(1), 79–96. https://doi.org/10.1016/0032-0633(81)90141-0

Coxon, J. C., & de Larquier, S. (2020). *johncoxon/tsyganenko: Version 2020.0.0*. Zenodo. https://doi.org/10.5281/zenodo.3937276

Coxon, J. C., Shore, R. M., Freeman, M. P., Fear, R. C., Browett, S. D., Smith, A. W., et al. (2019). Timescales of Birkeland currents driven by the IMF. *Geophysical Research Letters*, *46*(14), 7893–7901. https://doi.org/10.1029/2018gl081658

Davey, E. A., Lester, M., Milan, S. E., & Fear, R. C. (2012). Storm and substorm effects on magnetotail current sheet motion. *Journal of Geophysical Research*, *117*(A2). https://doi.org/10.1029/2011JA017112

Davey, E. A., Lester, M., Milan, S. E., Fear, R. C., & Forsyth, C. (2012). The orientation and current density of the magnetotail current sheet: A statistical study of the effect of geomagnetic conditions. *Journal of Geophysical Research*, *117*(A7). https://doi.org/10.1029/2012JA017715

Dungey, J. W. (1961). Interplanetary magnetic field and the auroral zones. *Physics Review Letters*, *6*, 47–48. https://doi.org/10.1103/physrevlett.6.47

Escoubet, C., Schmidt, R., & Goldstein, M. (1997). Cluster—Science and mission overview. In C. Escoubet, C. Russell, & R. Schmidt (Eds.), *The cluster and phoenix missions* (pp. 11–32). Springer Netherlands. https://doi.org/10.1007/978-94-011-5666-0_1

Escoubet, C. P., Fehringer, M., & Goldstein, M. (2001). The Cluster mission. *Annales Geophysicae*, *19*(10/12), 1197–1200. https://doi.org/10.5194/angeo-19-1197-2001

Fear, R. C. (2021). The northward IMF magnetosphere. In R. Maggiolo, N. André, H. Hasegawa, & D. T. Welling (Eds.), *Space physics and aeronomy collection volume 2: Magnetospheres in the solar system* (pp. 293–309). American Geophysical Union (AGU). https://doi.org/10.1002/9781119815624.ch19

Fear, R. C., & Milan, S. E. (2012a). The IMF dependence of the local time of transpolar arcs: Implications for formation mechanism. *Journal of Geophysical Research*, *117*(A3). https://doi.org/10.1029/2011JA017209

Fear, R. C., & Milan, S. E. (2012b). Ionospheric flows relating to transpolar arc formation. *Journal of Geophysical Research*, *117*(A9). https://doi.org/10.1029/2012ja017830

Fear, R. C., Milan, S. E., Carter, J. A., & Maggiolo, R. (2015). The interaction between transpolar arcs and cusp spots. *Geophysical Research Letters*, *42*(22), 9685–9693. https://doi.org/10.1002/2015gl066194

Fear, R. C., Milan, S. E., Maggiolo, R., Fazakerley, A. N., Dandouras, I., & Mende, S. B. (2014). Direct observation of closed magnetic flux trapped in the high-latitude magnetosphere. *Science*, *346*(6216), 1506–1510. https://doi.org/10.1126/science.1257377

Frank, L. A., Craven, J. D., Burch, J. L., & Winningham, J. D. (1982). Polar views of the Earth's aurora with Dynamics Explorer. *Geophysical Research Letters*, *9*(9), 1001–1004. https://doi.org/10.1029/gl009i009p01001

Frank, L. A., Craven, J. D., Gurnett, D. A., Shawhan, S. D., Weimer, D. R., Burch, J. L., et al. (1986). The theta aurora. *Journal of Geophysical Research*, *91*(A3), 3177–3224. https://doi.org/10.1029/ja091ia03p03177

Fryer, L. J., Fear, R. C., Coxon, J. C., & Gingell, I. L. (2021). Observations of closed magnetic flux embedded in the lobes during periods of northward IMF. *Journal of Geophysical Research: Space Physics*, *126*(6), e2021JA029281. https://doi.org/10.1029/2021JA029281

Gosling, J. T., Thomsen, M. F., Le, G., & Russell, C. T. (1996). Observations of magnetic reconnection at the lobe magnetopause. *Journal of Geophysical Research: Space Physics*, *101*(A11), 24765–24773. https://doi.org/10.1029/96ja02254

Goudarzi, A., Lester, M., Milan, S. E., & Frey, H. U. (2008). Multi-instrumentation observations of a transpolar arc in the Northern Hemisphere. *Annales Geophysicae*, *26*(1), 201–210. https://doi.org/10.5194/angeo-26-201-2008

Grocott, A., Cowley, S. W. H., & Sigwarth, J. B. (2003). Ionospheric flow during extended intervals of northward but -dominated IMF. *Annales Geophysicae*, *21*(2), 509–538. https://doi.org/10.5194/angeo-21-509-2003

Grocott, A., Yeoman, T. K., Milan, S. E., Amm, O., Frey, H. U., Juusola, L., et al. (2007). Multi-scale observations of magnetotail flux transport during IMF-northward non-substorm intervals. *Annales Geophysicae*, *25*(7), 1709–1720. https://doi.org/10.5194/angeo-25-1709-2007

Hosokawa, K., Kullen, A., Milan, S., Reidy, J., Zou, Y., Frey, H. U., et al. (2020). Aurora in the polar cap: A review. *Space Science Reviews*, *216*(1), 15. https://doi.org/10.1007/s11214-020-0637-3

Hunter, J. D. (2007). Matplotlib: A 2D graphics environment. *Computing in Science & Engineering*, *9*(3), 90–95. https://doi.org/10.1109/MCSE.2007.55

King, J. H., & Papitashvili, N. E. (2014). *One min and 5-min solar wind data sets at the Earth's bow shock nose*. Retrieved from http://omniweb.gsfc.nasa.gov/html/HROdocum.html

Laakso, H., Perry, C., McCaffrey, S., Herment, D., Allen, A., Harvey, C., et al. (2010). Cluster active archive: Overview. In H. Laakso, M. Taylor, & C. P. Escoubet (Eds.), *The cluster active archive* (pp. 3–37). Springer Netherlands. https://doi.org/10.1007/978-90-481-3499-1_1

Le, G., Russell, C. T., Gosling, J. T., & Thomsen, M. F. (1996). Isee observations of low-latitude boundary layer for northward interplanetary magnetic field: Implications for cusp reconnection. *Journal of Geophysical Research*, *101*(A12), 27239–27249. https://doi.org/10.1029/96ja02528

Ling, Y., Shi, Q., Shen, X.-C., Tian, A., Li, W., Tang, B., et al. (2018). Observations of kelvin-Helmholtz waves in the earth's magnetotail near the lunar orbit. *Journal of Geophysical Research: Space Physics*, *123*(5), 3836–3847. https://doi.org/10.1029/2018ja025183

Mende, S. B., Heetderks, H., Frey, H. U., Lampton, M., Geller, S. P., Abiad, R., et al. (2000). Far ultraviolet imaging from the image spacecraft. 2. Wideband fuv imaging. *Space Science Reviews*, *91*(1), 271–285. https://doi.org/10.1023/A:1005227915363

Mende, S. B., Heetderks, H., Frey, H. U., Lampton, M., Geller, S. P., Habraken, S., et al. (2000). Far ultraviolet imaging from the IMAGE spacecraft. 1. System design. *Space Science Reviews*, *91*(1), 243–270. https://doi.org/10.1023/A:1005271728567

Milan, S. E., Carter, J. A., & Hubert, B. (2020). Probing the magnetic structure of a pair of transpolar arcs with a solar wind pressure step. *Journal of Geophysical Research: Space Physics*, *125*(2), e2019JA027196. https://doi.org/10.1029/2019JA027196

Milan, S. E., Hubert, B., & Grocott, A. (2005). Formation and motion of a transpolar arc in response to dayside and nightside reconnection. *Journal of Geophysical Research*, *110*(A1). https://doi.org/10.1029/2004JA010835

Morley, S. K., Koller, J., Welling, D. T., Larsen, B. A., Henderson, M. G., & Niehof, J. T. (2010). SpacePy—A Python-based library of tools for the space sciences. In S. van der Walt, & J. Millman (Eds.), *Proceedings of the 9th Python in Science Conference (SciPy 2010)* (pp. 39–45). https://doi.org/10.25080/majora-92bf1922-00c

Nakamura, T. K. M., Eriksson, S., Hasegawa, H., Zenitani, S., Li, W. Y., Genestreti, K. J., et al. (2017). Mass and energy transfer across the earth's magnetopause caused by vortex-induced reconnection. *Journal of Geophysical Research: Space Physics*, *122*(11), 11505–11522. https://doi.org/10.1002/2017ja024346

Nakamura, T. K. M., Hasegawa, H., Daughton, W., Eriksson, S., Li, W. Y., & Nakamura, R. (2017). Turbulent mass transfer caused by vortex induced reconnection in collisionless magnetospheric plasmas. *Nature Communications*, *8*(1), 1582. https://doi.org/10.1038/s41467-017-01579-0

Ness, N. F., & Wilcox, J. M. (1964). Solar origin of the Interplanetary Magnetic Field. *Physical Review Letters*, *13*, 461–464. https://doi.org/10.1103/PhysRevLett.13.461

Panov, E. V., Nakamura, R., Baumjohann, W., Sergeev, V. A., Petrukovich, A. A., Angelopoulos, V., et al. (2010). Plasma sheet thickness during a bursty bulk flow reversal. *Journal of Geophysical Research: Space Physics*, *115*(A5). https://doi.org/10.1029/2009ja014743

Parker, E. N. (1957). Sweet's mechanism for merging magnetic fields in conducting fluids. *Journal of Geophysical Research*, *62*(4), 509–520. https://doi.org/10.1029/JZ062i004p00509

Parker, E. N. (1958). Dynamics of the interplanetary gas and magnetic fields. *The Astrophysical Journal*, *128*, 664. https://doi.org/10.1086/146579

Reidy, J. A., Fear, R. C., Whiter, D. K., Lanchester, B., Kavanagh, A. J., Milan, S. E., et al. (2018). Interhemispheric survey of polar cap aurora. *Journal of Geophysical Research: Space Physics*, *123*(9), 7283–7306. https://doi.org/10.1029/2017ja025153

Reidy, J. A., Fear, R. C., Whiter, D. K., Lanchester, B. S., Kavanagh, A. J., Paxton, L. J., et al. (2017). Multi-instrument observation of simultaneous polar cap auroras on open and closed magnetic field lines. *Journal of Geophysical Research: Space Physics*, *122*(4), 4367–4386. https://doi.org/10.1002/2016ja023718

Reidy, J. A., Fear, R. C., Whiter, D. K., Lanchester, B. S., Kavanagh, A. J., Price, D. J., et al. (2020). Multiscale observation of two polar cap arcs occurring on different magnetic field topologies. *Journal of Geophysical Research: Space Physics*, *125*(8), e2019JA027611. https://doi.org/10.1029/2019JA027611

Rème, H., Aoustin, C., Bosqued, J. M., Dandouras, I., Lavraud, B., Sauvaud, J. A., et al. (2001). First multispacecraft ion measurements in and near the Earth's magnetosphere with the identical Cluster ion spectrometry (CIS) experiment. *Annales Geophysicae*, *19*(10/12), 1303–1354. Retrieved from https://hal.archives-ouvertes.fr/hal-00329192

Shepherd, S. G. (2014). Altitude-adjusted corrected geomagnetic coordinates: Definition and functional approximations. *Journal of Geophysical Research: Space Physics*, *119*(9), 7501–7521. https://doi.org/10.1002/2014ja020264

Shi, Q. Q. (2019). Solar wind entry into the lobe and the related polar cap auroral arc growing. In *AGU fall meeting abstracts SM51C–3211*.

Shi, Q. Q., Zong, Q.-G., Fu, S. Y., Dunlop, M. W., Pu, Z. Y., Parks, G. K., et al. (2013). Solar wind entry into the high-latitude terrestrial magnetosphere during geomagnetically quiet times. *Nature Communications*, *4*(1), 1466. https://doi.org/10.1038/ncomms2476

Song, P., & Russell, C. T. (1992). Model of the formation of the low-latitude boundary layer for strongly northward interplanetary magnetic field. *Journal of Geophysical Research: Space Physics*, *97*(A2), 1411–1420. https://doi.org/10.1029/91ja02377

Sorathia, K. A., Merkin, V. G., Ukhorskiy, A. Y., Allen, R. C., Nykyri, K., & Wing, S. (2019). Solar wind ion entry into the magnetosphere during northward IMF. *Journal of Geophysical Research: Space Physics*, *124*(7), 5461–5481. https://doi.org/10.1029/2019ja026728

Tenfjord, P., Østgaard, N., Snekvik, K., Laundal, K. M., Reistad, J. P., Haaland, S., & Milan, S. E. (2015). How the IMF induces a component in the closed magnetosphere and how it leads to asymmetric currents and convection patterns in the two hemispheres. *Journal of Geophysical Research: Space Physics*, *120*(11), 9368–9384. https://doi.org/10.1002/2015JA021579

Tsyganenko, N. A. (1996). Effects of the solar wind conditions in the global magnetospheric configurations as deduced from data-based field models. In E. J. Rolfe, & B. Kaldeich (Eds.), *International conference on substorms* (Vol. 389, p. 181).

van der Walt, S., Colbert, S. C., & Varoquaux, G. (2011). The NumPy array: A structure for efficient numerical computation. *Computing in Science & Engineering*, *13*(2), 22–30. https://doi.org/10.1109/MCSE.2011.37

Woch, J., & Lundin, R. (1992). Signatures of transient boundary layer processes observed with viking. *Journal of Geophysical Research*, *97*(A2), 1431–1447. https://doi.org/10.1029/91ja02490

Xing, Z., Zhang, Q., Han, D., Zhang, Y., Sato, N., Zhang, S., et al. (2018). Conjugate observations of the evolution of polar cap arcs in both hemispheres. *Journal of Geophysical Research: Space Physics*, *123*(3), 1794–1805. https://doi.org/10.1002/2017ja024272

Zhu, L., Schunk, R., & Sojka, J. (1997). Polar cap arcs: A review. *Journal of Atmospheric and Solar-Terrestrial Physics*, *59*(10), 1087–1126. https://doi.org/10.1016/s1364-6826(96)00113-7